Optimal dynamic soaring consists of successive shallow arcs

Gabriel D. Bousquet[1], Michael S. Triantafyllou, Jean-Jacques E. Slotine

Department of Mechanical Engineering, Massachusetts Institute of Technology,
Cambridge, MA, 02139, USA

ST1 Numerical solution by direct collocation

Numerical procedure

Our numerical model for figures 4 to 7 is based on the EOM of equation (3) with $w(z) = \frac{w_0}{1+\exp{-z/\delta}}$. We formally rewrite the EOM $\dot{\mathbf{x}} = f(\mathbf{x}, \mathbf{u})$. The question that we want answered is the following: *For a given glider ($c_{D,0}, f_{\max}$) and a given shear layer thickness δ, what is the minimum wind speed inhomogeneity parameter w_0 that has feasible trajectories, periodic in the state $\mathbf{x}$?* More specifically, for the traveling trajectories (right-hand side of figure 4 and figure 6), the boundary conditions are $V(T) = V(0), \psi(T) = \psi(0), \gamma(T) = \gamma(0), z(T) = z(0)$. For the circular trajectories (left-hand side of figure 4, we imposed the boundary conditions $V(T) = V(0), \psi(T) = \psi(0) + 2\pi, \gamma(T) = \gamma(0), z(T) = z(0), x(T) = x(0)$. Note that the x-constraint in the latter set of boundary conditions is not strictly required. Without it the upper half cycle tends to peak at a higher altitude, with very small airspeed and very large c_L. The x-constraint maintains c_L to realistic values while conserving the main features of the unconstrained trajectories.

The question is cast into a finite dimensional optimization problem by direct collocation. First, time over one period T is discretized into time steps $[0, n_1T, n_2T, \ldots, n_{N-1}T, T]$ with $0 < n_1 < \cdots < n_{N-1} < 1$. The spacing need not be uniform. We use the shorthand $\mathbf{x}_i \hat{=} \mathbf{x}(n_iT), \mathbf{u}_i = \mathbf{u}(n_iT)$. Following *e.g.* [24, 37], the continuous-time constraints $\mathbf{x}(n_iT) = \int_{n_{i-1}T}^{n_iT} f(\mathbf{x}(t), \mathbf{u}(t))dt$ are approximated by

$$\mathbf{u}_{m_i} = \frac{1}{2}(\mathbf{u}_i + \mathbf{u}_{i-1})$$

$$\mathbf{x}_{m_i} = \frac{1}{2}(\mathbf{x}_i + \mathbf{x}_{i-1}) - \frac{1}{8}(f(\mathbf{x}_i, \mathbf{u}_i) - f(\mathbf{x}_{i-1}, \mathbf{u}_{i-1}))(n_i - n_{i-1})T$$

$$0 = \mathbf{C}_i = \mathbf{x}_{i-1} + \frac{1}{6}\left(f(\mathbf{x}_i, \mathbf{u}_i) + 4f(\mathbf{x}_{m_i}, \mathbf{u}_{m_i}) + f(\mathbf{x}_{i-1}, \mathbf{u}_{i-1})\right)(n_i - n_{i-1})T$$

[1]g_b@mit.edu

For the traveling problem, the previous discretization leads to the following nonlinear program (NLP):

$$\underset{\mathbf{x}_0,\ldots,\mathbf{x}_N,\mathbf{u}_0,\ldots,\mathbf{u}_N,w_0,T}{\text{minimize}} \quad w_0$$

$$\begin{aligned}
\text{subject to} \quad & \mathbf{C}_i = 0, \quad i = 1,\ldots,N \\
& (V_N, \psi_N, \gamma_N, z_N) = (V_0, \psi_0, \gamma_0, z_0) \\
\text{and} \quad & z_0 = 0 \\
& V_i, c_{L,i} > 0 \\
& -\pi < \psi_i < \pi, \quad -\pi/2 < \gamma_i < \pi/2
\end{aligned} \tag{13}$$

A solution to the NLP is a feasible trajectory that locally minimizes the wind required for flight. Note that the last three relations are purely technical and the inequalities constraints were not active upon solution convergence.

Similarly, the circular problem is cast into

$$\underset{\mathbf{x}_0,\ldots,\mathbf{x}_N,\mathbf{u}_0,\ldots,\mathbf{u}_N,w_0,T}{\text{minimize}} \quad w_0$$

$$\begin{aligned}
\text{subject to} \quad & \mathbf{C}_i = 0, \quad i = 1,\ldots,N \\
& (V_N, \psi_N, \gamma_N, z_N, x_N) = (V_0, \psi_0 + 2\pi, \gamma_0, z_0, x_0) \\
\text{and} \quad & z_0 = 0 \\
& V_i, c_{L,i} > 0 \\
& -3\pi < \psi_i < 3\pi, \quad -\pi/2 < \gamma_i < \pi/2
\end{aligned} \tag{14}$$

The problem was then solved for various $(c_{D,0}, f_{\max}, \delta)$ with a nonlinear solver *e.g.* SNOPT. We typically used $N = 140$ time steps, leading to $O(1000)$ variables and constraints. Our Python implementation converged in $O(1-10)$ minutes on a 2013 Macbook Pro. We used more time steps than in similar studies. The main reason for this choice is that for small δ the transition through the shear layer is of short duration, and resolving it requires a high level or granularity. To reach very small values of δ and validate the convergence of our numerical model to our analytic model, we leveraged on the possibility to utilize non-uniform time spacing: we started by solving problems with large δ and subsequently addressed smaller δ by adaptively refining the time spacing near the transition in order to maintain a sufficient resolution.

Results

The raw results for the cases illustrated in figure 4 are collected in figures S2–S4 and S5–S7 and their characteristics are displayed in figures 6 and 7. For case with $\delta = 1/64$ and $1/2048$, the control points are non-uniformly spaced and are denser near the transition $z = 0$. For both the circular and traveling cases, $\delta = 1/64$ and $1/2048$ are qualitatively
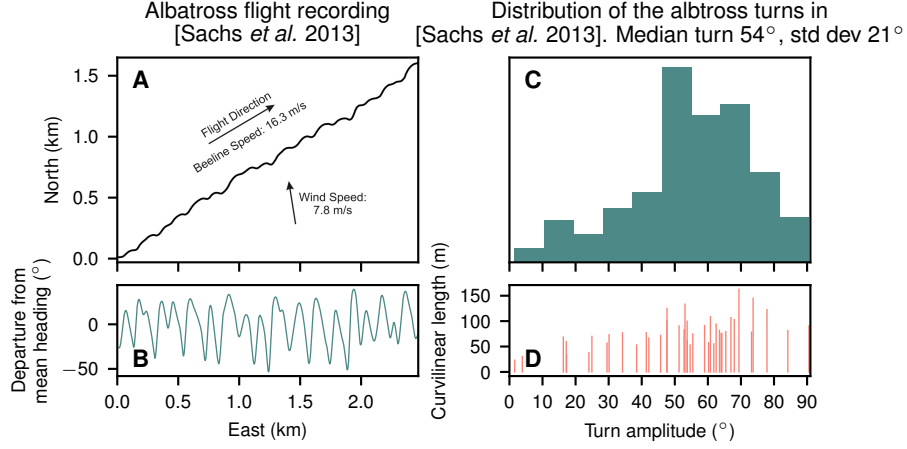
Figure S1: **Analysis of the albatross' trajectory**. (**a**) Recording of an albatross travelling across a low wind [22]. (**b**) Albatross heading along the trajectory. In (**c**) the statistical analysis of the flight shows that the albatross' median turns is 54° (mean 50°). In this particular recording, the albatross virtually never turns more than 90°. (**d**) Curvilinear length of the individual turns.

similar. The boundary thickness for the albatross is closest to case $\delta = 1/64$. For the traveling cases $\delta = 1/64$ and $1/2048$, the sub-periodicity discussed in section 3.2 is visible—a qualitative difference from $\delta = 2$. In contrast, all circular cases are qualitatively similar to each other across the range of δ's.

Figures S8–S11 show the minimum-wind trajectories in a wind field of the form $W(z) = W_0 \left(2 + \frac{1}{1+\exp -z/\delta} \right)$. In those cases, the aerodynamic quantities are unchanged, but the overall trajectory is convected at an additional speed $2W_0$. This models instances where the glider may access a boundary layer where the wind is only partially slowed down, as is the case in practice.

ST2 GPS data analysis

Sachs *et al.* recordings

The data for figures 2 and 6 were extracted from the bitmap figure 9A of [22] (reproduced in figure S1a). For each pixel in the East direction, the centre of the trajectory line was determined by an average operation. The result was filtered with the `filtfilt` filter from `scipy.signal`. The (ground) heading angle was then calculated (figure S1b). Figure S1c,d reports the distribution of the turns in the recording.

Yonehara *et al.* recordings

Yohehara *et al.* [23] contain latitude–longitude time histories of wandering albatrosses (*Diomedea exulans*). The tracks are sampled at 1 Hz and for the tracks of interest in the present study (albatrosses 1 and 4), the recording is about 48h long, with periods of flight, foraging, and rest on water.

The latitude–longitude data is first converted to distances by projection with Python's `Basemap` cylindrical equidistant projection centred at (47° East, 43° South). The trajectory is then interpolated at 5 Hz with a cubic spline using Python's `interp1d`. Each point is attributed a heading angle by centred finite difference of the positions at 5 Hz. A search for local extrema is performed on the unwrapped heading angle. Because the cubic spline introduces some oscillation in the trajectory in some places, if local maxima and minima follow each other by less than 2.5 s, they are merged together and replaced by a single point of average heading. This technique was chosen over linear interpolation or filtering as both reduce peaks in heading angles and would underestimate the amplitude of turns. The obtained time history of local minima and maxima of heading angle were used to obtain the sequence of turn amplitudes.

The data points when the groundspeed was outside the 5–50 m/s range were removed, as they tend to represent either phases where the albatross is resting on water, or unrealistic GPS recordings. We also set aside the turns of amplitude greater than 360° which are concentrated within periods of active foraging (they account for about 1% of the turns).

For albatross #4, a further step was taken. We started with the long westward flight of Albatross #4 (approximately 650 km on March 18, 2007 from 6:02AM to 4:37PM). Along the travel sequence, there are a few instances where the albatross seemed to be foraging (not making progress for significant stretches of time), or when the GPS recording was spotty (unrealistic and sporadic jumps in the data). For this reason, we removed 5 time intervals, varying in duration from 2 to 47 min, for a total of 1h47. The resulting tracks are shown in figure 3.

Empirical Analysis

The sample standard deviation is 21° and 32° for Sachs' albatross and Yonehara's albatross #4, respectively. With 40 and 3,680 samples respectively, within the approximation of the central limit theorem, the standard deviation of the sample mean pdf is 3.3 and 0.5°, respectively.

Our numerical model predicts a typical turn angle of 80°. Compared to the half-turn description (null hypothesis), the log-likelihood ratio based on the t-test pdf is 102 for Sachs' albatross ($p < 10^{-23}$) and $4 \cdot 10^4$ for Yonehara's albatross #4 ($p < 10^{-300}$). In view of the data from albatross #4, the prediction of our numerical model is 10^{8700} times more likely than the half-turn's.

ST3 Comparison with log-based numerical approaches

In figures 6 and 7, we compare our models with existing numerical literature in a log profiles. [33] was chosen because it is the first full trajectory optimization in a log field (precisely, a power law) in our knowledge. It is also used as a validation case in [25]. [24] compares 3 DoF, 6 DoF, and panel-based aircraft models and is a the most complete study, in our knowledge, of the sensitivity of the minimum-wind trajectory in a log profile, therefore constituting a reference for assessing relative significance of mismatches and sensitivities.

Both references consider the minimum-wind trajectory in a log (or power law) wind profile, and set a minimum authorized minimum altitude (or wing-tip clearance from the water). In order to compare with our own model and extract an equivalent shear layer, we measured on in both cases the thickness $\Delta_{80\%}$ such that

$$\frac{W(z_{\min} + \Delta_{80\%}) - W(z_{\min})}{W(20\text{m}) - W(z_{\min})} = 80\%$$

and converted that value back into the non-dimensional shear layer parameter δ. Overall, the quantities used for comparison are collected in Table S1.

While both studies attempt to model a glider over a similar hypothetical shear layer above the ocean surface, they lead to a somewhat different shear layer parameter δ because the wing-loadings considered are different. Overall, despite model differences (for instance, our model does not enforce a maximum lift coefficient), the results all agree well with each other. In particular, the sensitivity of the minimum-wind trajectory with respect to the wind parameterization, whether logarithmic, or modelled with a logistic function, is small, validating our approach.

Finally, as also mentioned in the article, the natural frame of reference in which to analyse the minimum-wind problem is the frame convected with the average wind (for instance approximately $w(z = 0)$ in our model, or $(W(z_{\min}) + W(z_{\max}))/2$ in a log profile). There, the problem's symmetry is maximized and the trajectory is simplified. Within their respective models, [24, 33] underline the fact that because the glider is forbidden to reach the no-wind region which is confined to the very surface, only 25–35% of the range of wind may in fact be accessed. In our model, this could modelled by considering the wind profile

$$W(z) = W_0 \left(n + \frac{1}{1 + \exp -z/\delta} \right)$$

where $n \approx 2 - 3$ is some multiplicative factor reflecting that the wind speed in the lower layer is non-zero. Equivalently, this amounts to considering that the trajectory is convected downstream at an additional rate nW_0. The trajectories in this configuration are represented in figures S8–S11. Note that the trajectory in S8 is extremely similar to that in [33], for a similar shear layer thickness. Likewise, the trajectory in figure S11 (and previous figures) is similar to that of the albatross in figure 2, suggesting again the

probable ability of the albatross to reach the slow and separated regions behind waves. Statistical analysis of the albatross' height during dynamic soaring would help validate and/or refine this hypothesis.

ST4 Complements on the thin shear layer regime analytic model

In the thin shear layer limit, let ψ_0 and v_0 be the air-relative heading and speeds at altitude $z = 0$ *i.e.* centred in the middle of the shear layer. Define $\bar{\psi} = (\psi^+ + \psi^-)/2$, $\bar{v} = (v^+ + v^-)/2$ and $\Delta v = v^+ - v^-$. Assume periodic (energy neutral) conditions. If f and c_L are kept constant, the evolution of airspeed during glide in equation (5) can be rewritten as

$$\int_{v_+}^{v^-} \sqrt{1 - \frac{1}{c_L^2 v^4}} \frac{dv}{v} = -\frac{1}{f} \int_{\psi_n^+}^{\psi_{n+1}^-} d\psi. \tag{15}$$

Integrate the left-hand side with the third order accurate midpoint approximation at $\bar{v}$. Integrate the right-hand side and recall that due to the antisymmetry of the equations, the turn amplitude of the glide phase is $2\bar{\psi}$. This gives

$$\sqrt{1 - \frac{1}{c_L^2 \bar{v}^4}} \frac{\Delta v}{\bar{v}} + O(\Delta v^3) = \frac{2}{f} \bar{\psi}. \tag{16}$$

The relations of transition for the heading are:

$$\tan \psi^+ = \tan \psi_0 + \frac{w_0}{2v_0 \cos \psi_0}$$
$$\tan \psi^- = \tan \psi_0 - \frac{w_0}{2v_0 \cos \psi_0}. \tag{17}$$

The relations of transition for the airspeed are

$$v^+ = v_0 \sqrt{1 + \frac{w_0}{v_0} \sin \psi_0 + \left(\frac{w_0}{2v_0}\right)^2}$$
$$v^- = v_0 \sqrt{1 - \frac{w_0}{v_0} \sin \psi_0 + \left(\frac{w_0}{2v_0}\right)^2}. \tag{18}$$

The following Taylor expansions follow:

$$\bar{\psi} = \psi_0 + O\left(\left(\frac{w_0}{v_0 \cos \psi_0}\right)^2\right) \tag{19a}$$

$$\bar{v} = v_0 \left\{1 + O\left(\left(\frac{w_0}{v_0}\right)^2\right)\right\} \tag{19b}$$

$$\Delta v_{\text{transition}} = w_0 \sin \psi_0 + O\left(\frac{w_0^3}{v_0^2}\right). \tag{19c}$$

Below we assume that v_0, ψ_0 are fixed, and express the residuals in terms of w_0. The residual in equation (16) can now be transformed with equation (19c) to $\Delta v = O(w_0)$, and the quantities $\bar{\psi}$ and $\bar{v}$ can be replaced with ψ_0 and v_0 at the price of a $O(w_0^2)$ error. The equation of glide becomes

$$\alpha_0 \frac{\Delta v}{v_0} = \frac{2}{f}\psi_0 + O(w_0^2)$$

with $\alpha_0 = \sqrt{1 - \frac{1}{c_L^2 v_0^4}}$. This is equation (7) where the approximation is exhibited. Combining it with the equation of transition (19c), the balance between airspeed gains and losses is

$$\alpha_0 \frac{w_0 \sin \psi_0}{v_0} = \frac{2}{f}\psi_0 + O(w_0^2)$$

which is similar to equation (9). Note that for any triplet (v_0, w_0, ψ_0) such that equation (15) is integrable, and $\bar{\psi}$ is not strictly 0, the equation has a solution if f can be chosen arbitrarily.

For any given fixed ψ_0, v_0, now decrease w_0 (equivalently, increase f). The residual in w_0^2 is dominated and the equation converges to

$$\frac{v_0}{\alpha_0} = \frac{\sin \psi_0}{\psi_0} \frac{f}{2} w_0 \tag{20}$$

i.e. equation (9).

References

22. Sachs, G., Traugott, J., Nesterova, A. P. & Bonadonna, F. Experimental verification of dynamic soaring in albatrosses. *The Journal of experimental biology* **216,** 4222–32 (Nov. 2013).

23. Yonehara, Y. *et al.* Data from: Flight paths of seabirds soaring over the ocean surface enable measurement of fine-scale wind speed and direction. *Dryad, doi:10.5061/dryad.3pb86* (2016).

	Sachs 1993 [33]	Flanzer 2012 [24]
V_c (m/s)	14.9	8.2
$\left(c_L^{3/2}/c_D\right)_{\text{max}}$	24.2	19.4
W^* (m/s)	3.8	3.2 ± 0.1
δ (non-dim.)	0.075 ± 0.05	0.18 ± 0.01
$\Delta_{80\%}$ (m)	10	7.3
$z_{\text{max}} - z_{\text{min}}$ (m)	19.2	11.5
V_{max} (m/s)	21.5 ± 0.5	16 ± 1
t^* (s)	7.2	5.5 ± 0.5

Table S1: **Minimum-wind trajectory in a logarithmic wind** as reported by [24, 33]. ($z_{\text{max}} - z_{\text{min}}$) represents the distance between the maximum and minimum altitudes reached by the glider over one cycle. Note that also the physical boundary layer thickness is comparable in both studies, because of a smaller wing loading, upon non-dimensionalisation is appear thicker in [24].

24. Flanzer, T. C., Bunge, R. A. & Kroo, I. M. *Efficient Six Degree of Freedom Aircraft Trajectory Optimization with Application to Dynamic Soaring* in *AIAA Aviation Technology, Integration, and Operations Conference* (Indianapolis, Indiana, 2012).

25. Deittert, M., Richards, A., Toomer, C. A. & Pipe, A. Engineless Unmanned Aerial Vehicle Propulsion by Dynamic Soaring. *Journal of Guidance, Control, and Dynamics* **32,** 1446–1457 (Sept. 2009).

33. Sachs, G. Minimaler Windbedarf für den dynamischen Segelflug der Albatrosse. *Journal für Ornithologie* **134,** 435–445 (1993).

37. Hargraves, C. R. & Paris, S. W. Direct Trajectory Optimization Using Nonlinear Programming and Collocation. *AIAA J. Guidance* **10,** 338–342 (1987).
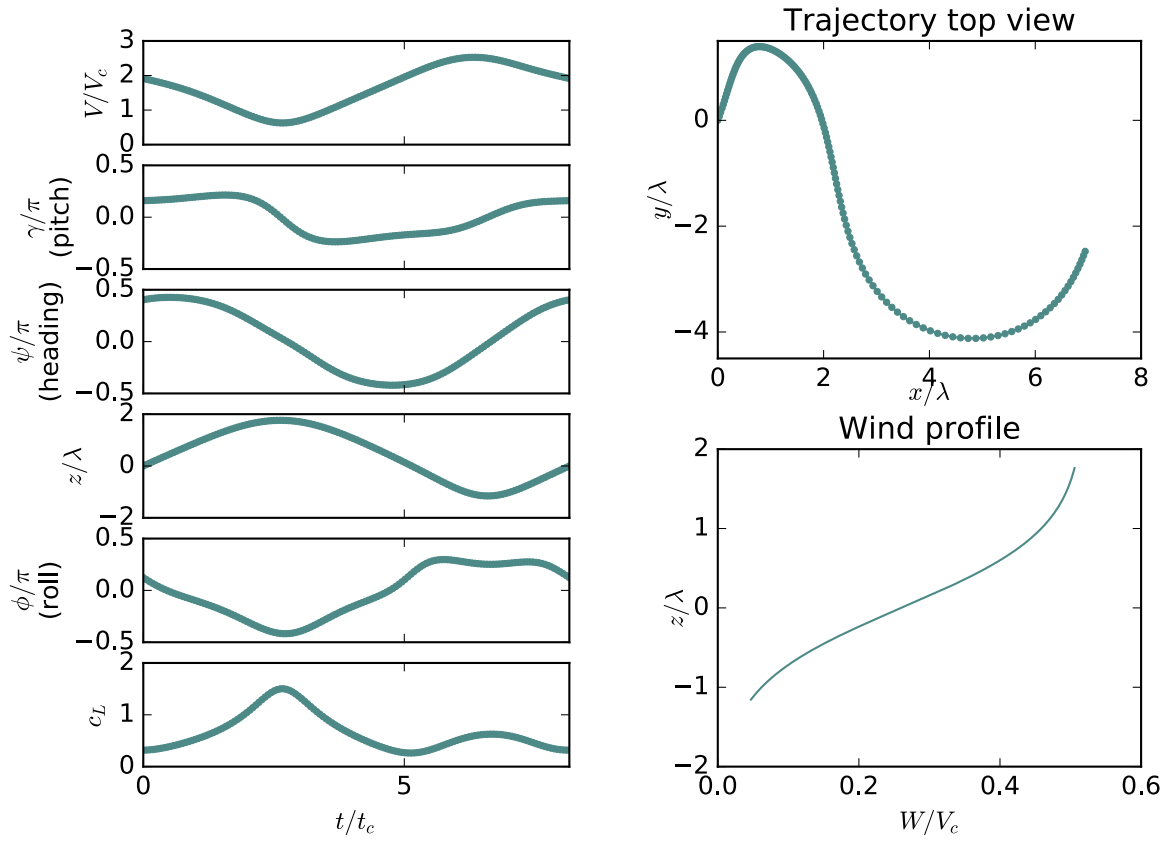
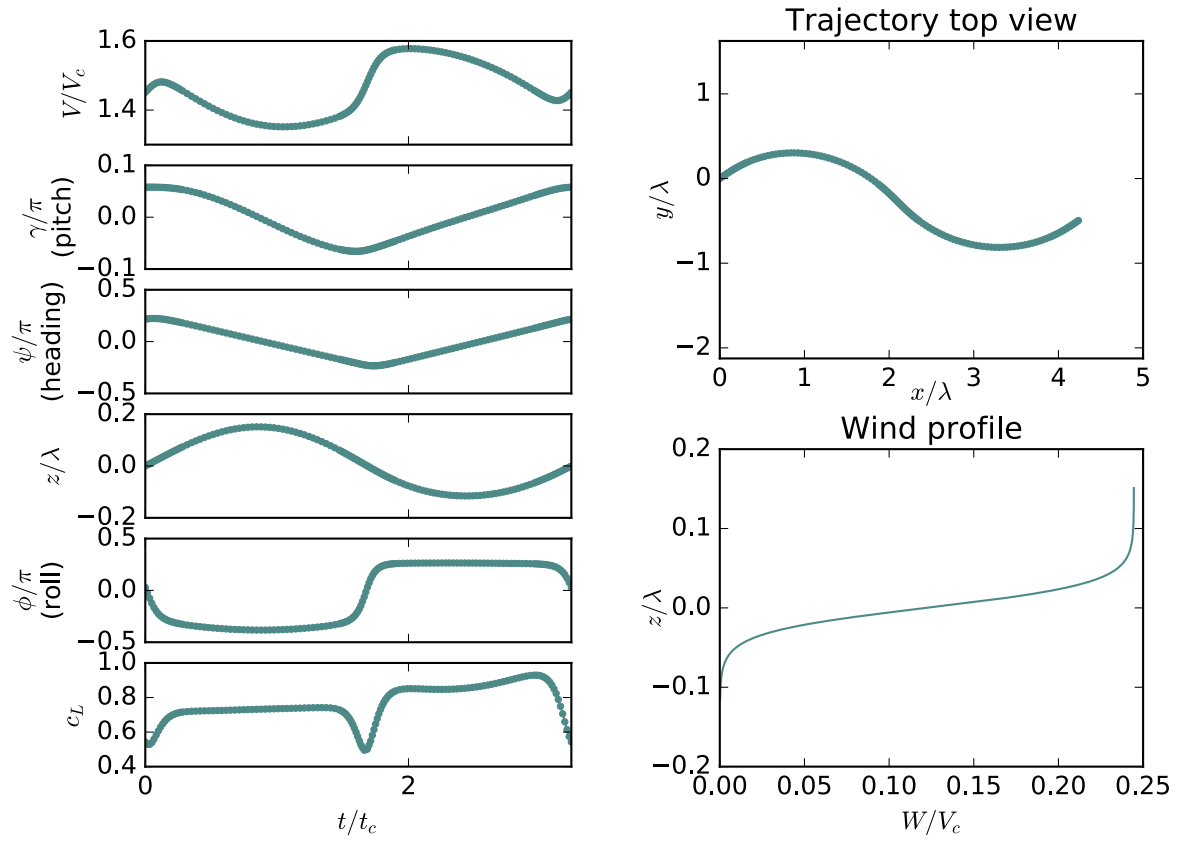Figure S2: **Solution to the Rayleigh problem** for $f_{\max} = 20, c_{L,f_{\max}} = 0.5, \delta = \lambda/2$. $w_0 = 0.52$.

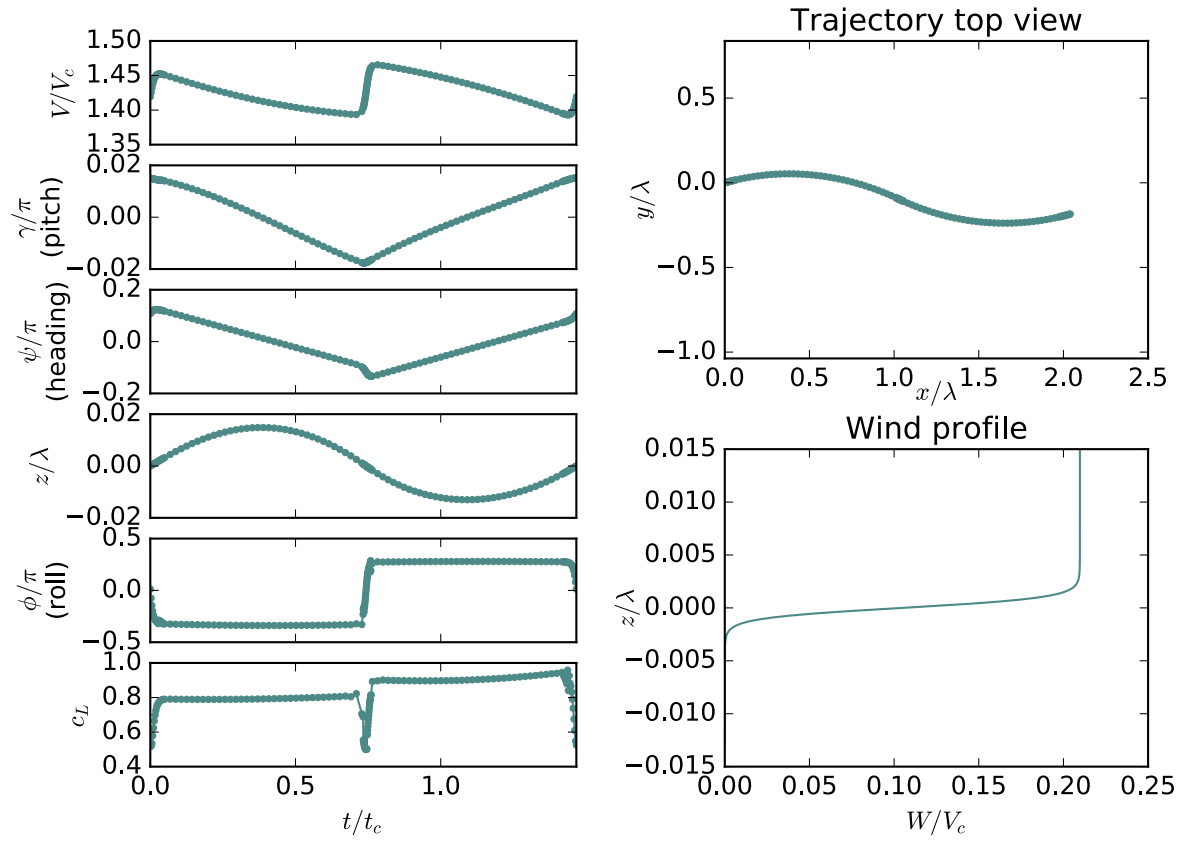Figure S3: **Solution to the Rayleigh problem** for $f_{\max} = 20, c_{L,f_{\max}} = 0.5, \delta = \lambda/64$. $w_0 = 0.24$.

Figure S4: **Solution to the Rayleigh problem** for $f_{\max} = 20, c_{L,f_{\max}} = 0.5, \delta = \lambda/2048$. $w_0 = 0.21$.

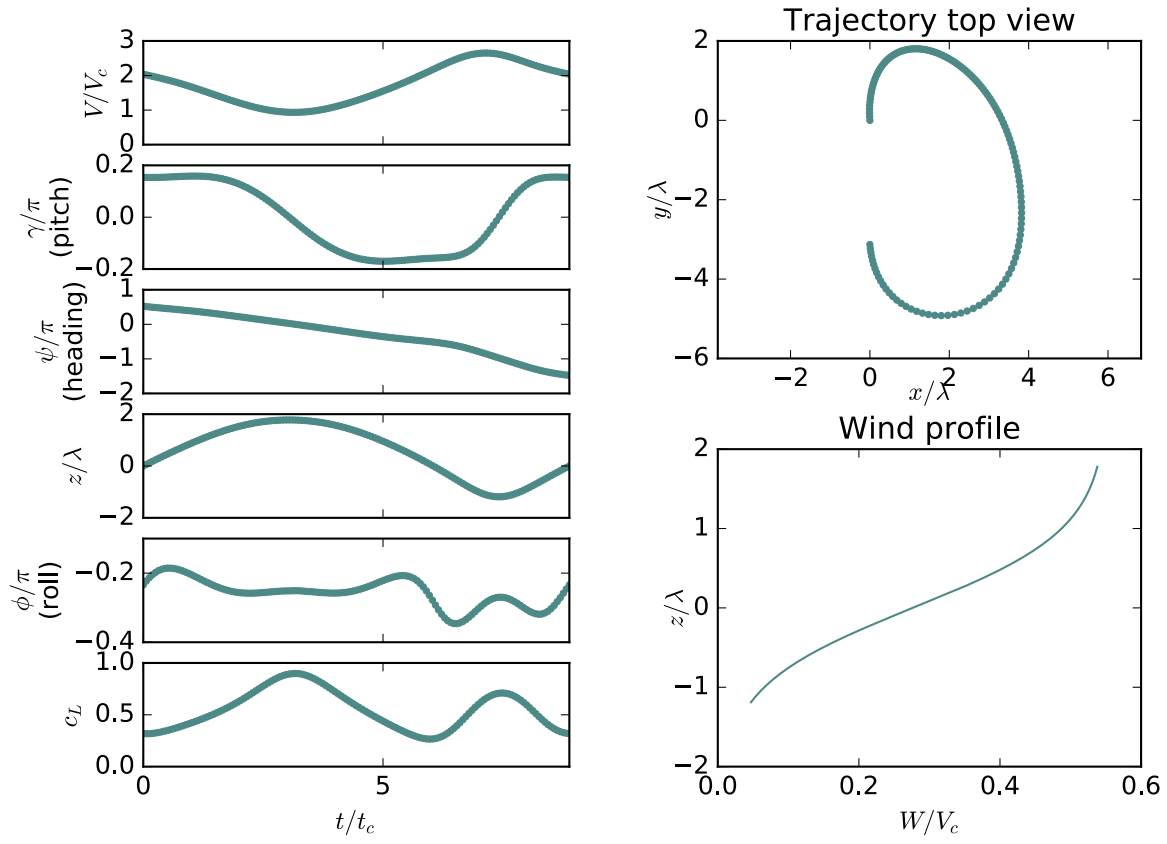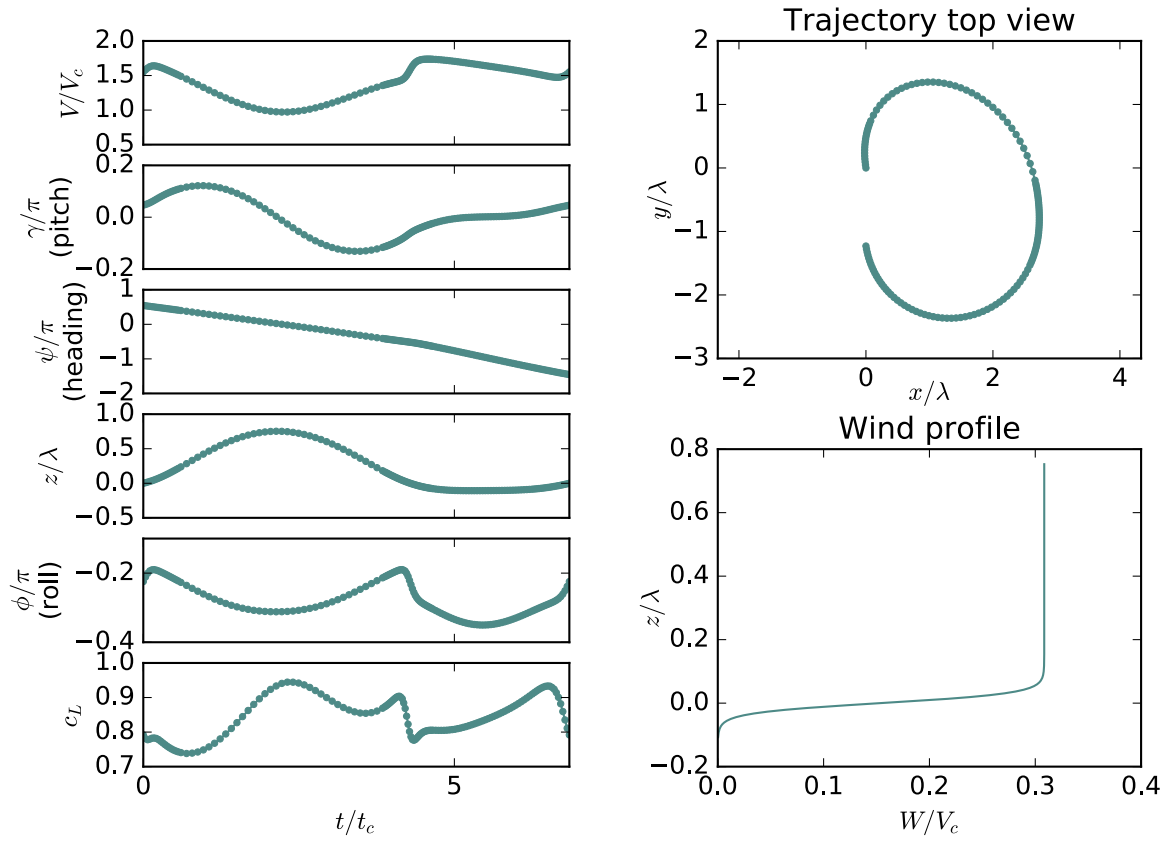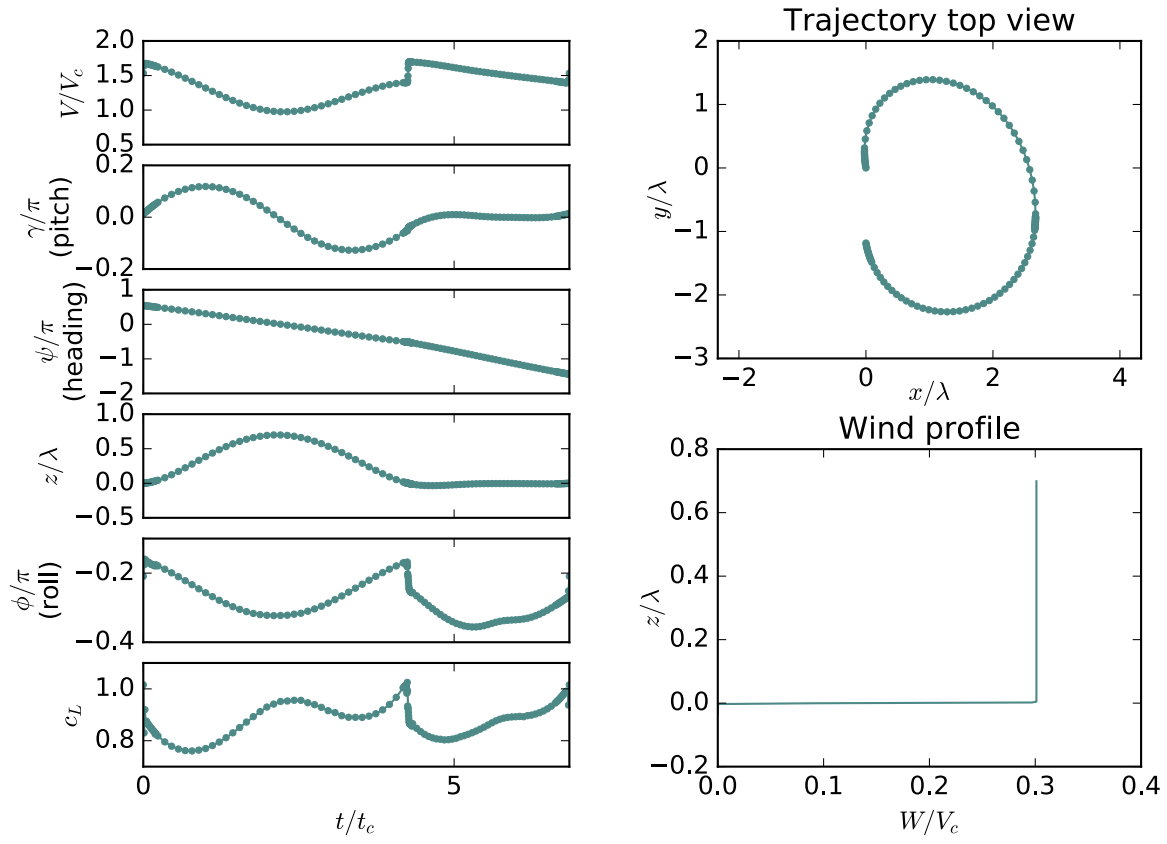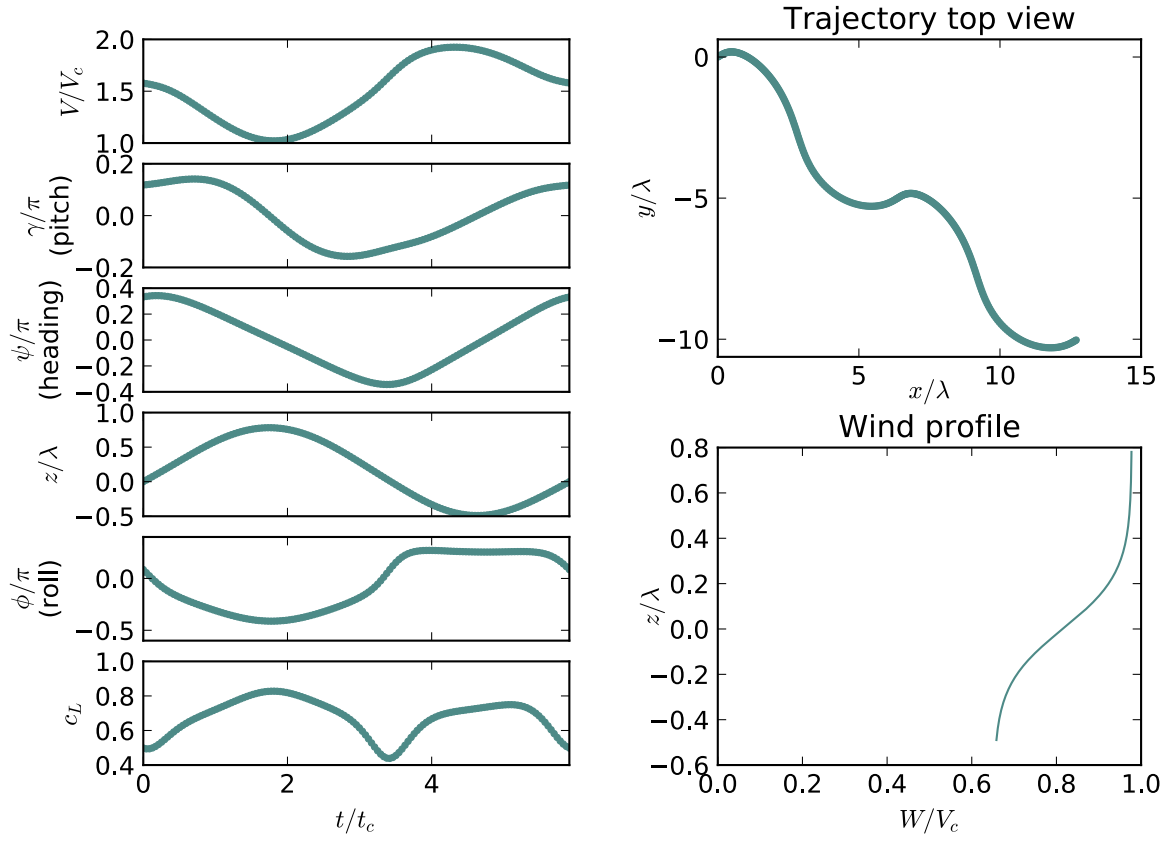Figure S5: **Solution to the Rayleigh problem** for $f_{\max} = 20, c_{L,f_{\max}} = 0.5, \delta = \lambda/2$. $w_0 = 0.55$.

Figure S6: **Solution to the Rayleigh problem** for $f_{\max} = 20, c_{L,f_{\max}} = 0.5, \delta = \lambda/64,$ $w_0 = 0.308.$

Figure S7: **Solution to the Rayleigh problem** for $f_\mathrm{max} = 20, c_{L,f_\mathrm{max}} = 0.5, \delta = \lambda/2048,$ $w_0 = 0.301$.

Figure S8: **Solution to the Rayleigh problem** for $f_{\max} = 20, c_{L,f_{\max}} = 0.5, \delta = \lambda/8$, in a wind $W(z) = W_0 \left(2 + \frac{1}{1+\exp -z/\delta}\right)$. The constant term in the wind definition, while having no effect on air-relative quantities, illustrates how the trajectory is overall convected downwind if the slow layer has a non-zero velocity.
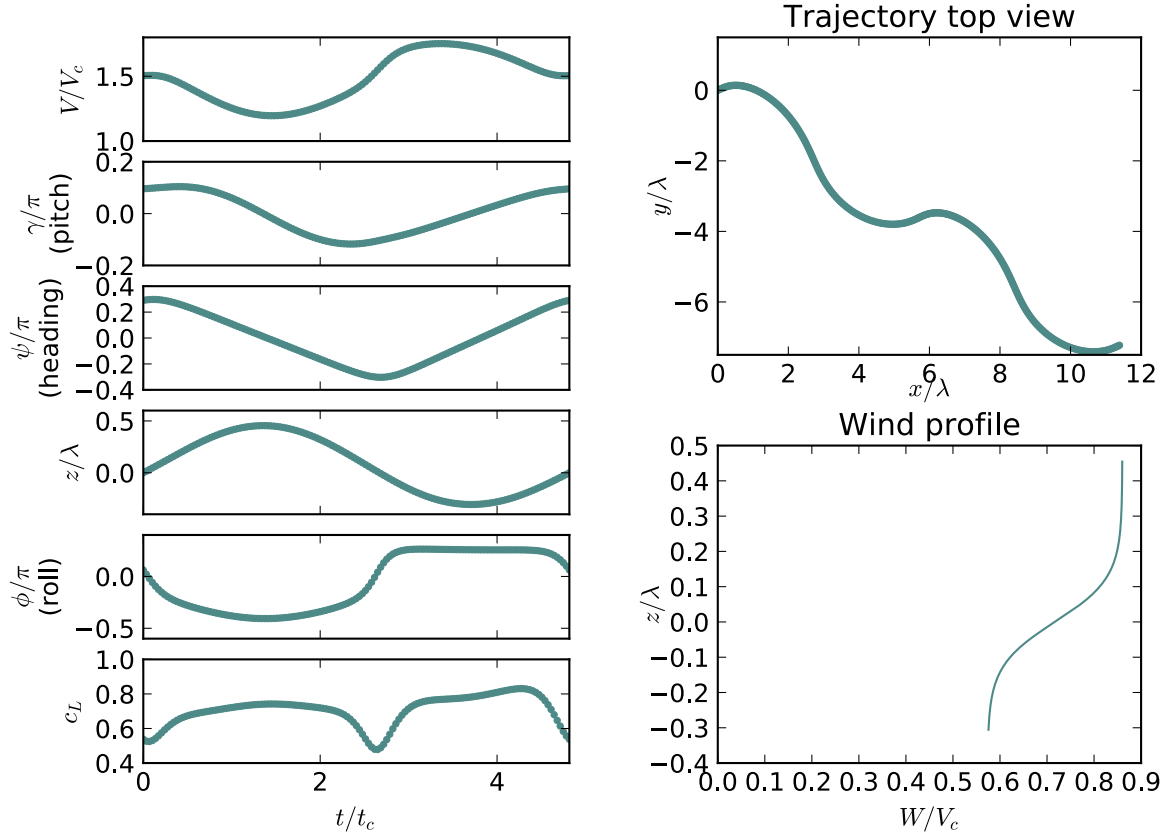
Figure S9: **Solution to the Rayleigh problem** for $f_{\max} = 20, c_{L,f_{\max}} = 0.5, \delta = \lambda/16$, in a wind $W(z) = W_0 \left(2 + \frac{1}{1 + \exp{-z/\delta}}\right)$. The constant term in the wind definition, while having no effect on air-relative quantities, illustrates how the trajectory is overall convected downwind if the slow layer has a non-zero velocity.
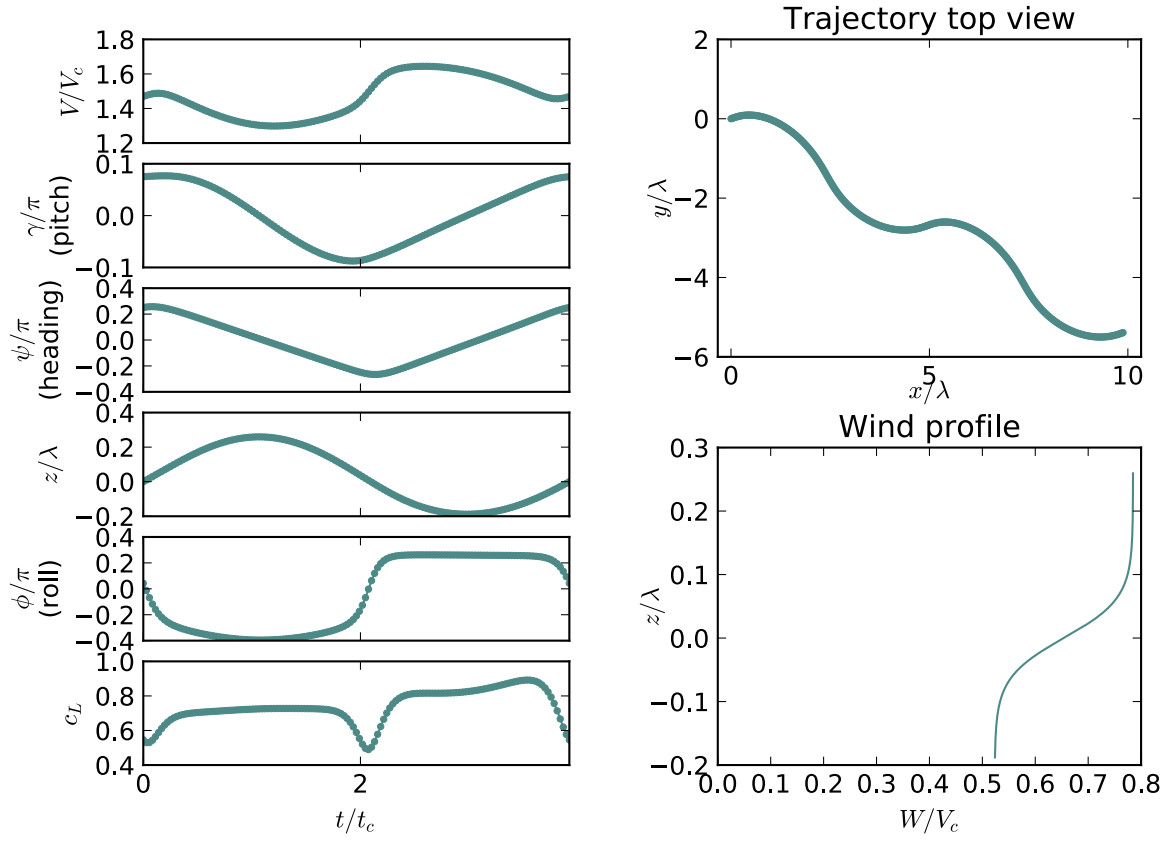
Figure S10: **Solution to the Rayleigh problem** for $f_{\max} = 20, c_{L,f_{\max}} = 0.5, \delta = \lambda/32$, in a wind $W(z) = W_0 \left(2 + \frac{1}{1+\exp -z/\delta} \right)$. The constant term in the wind definition, while having no effect on air-relative quantities, illustrates how the trajectory is overall convected downwind if the slow layer has a non-zero velocity.
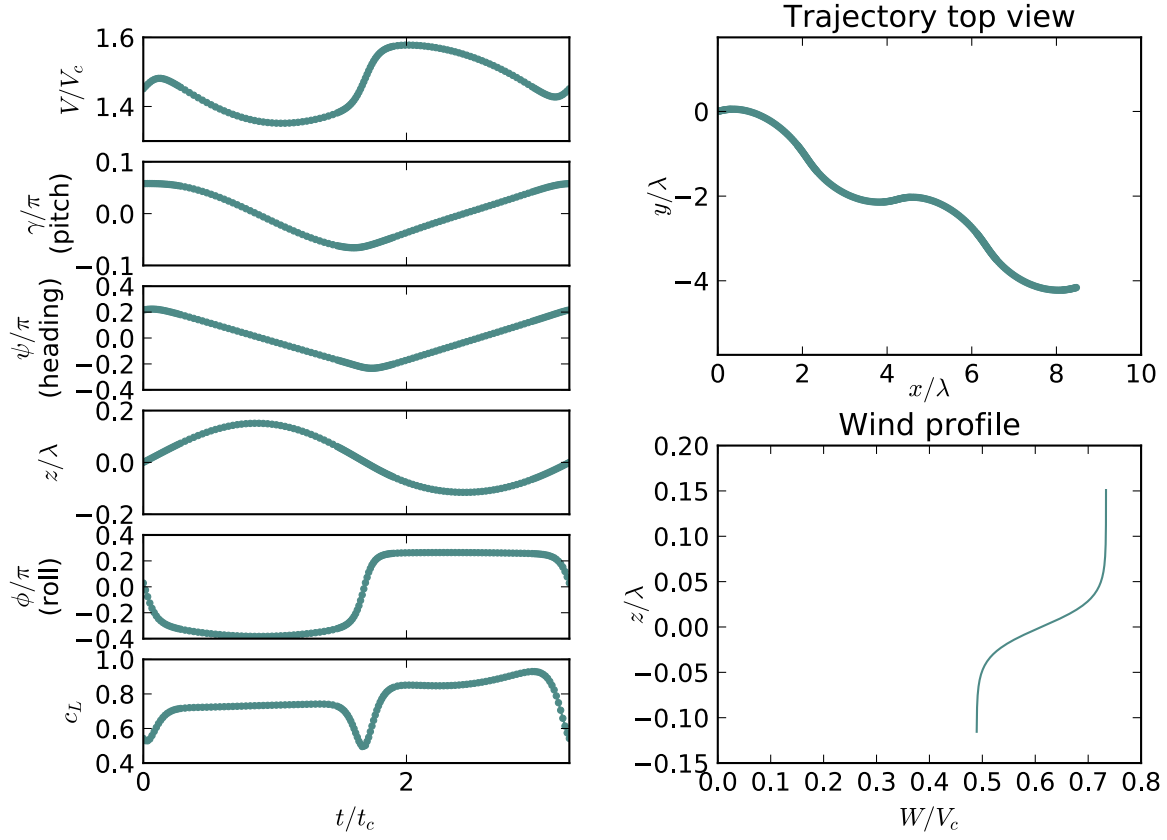
Figure S11: **Solution to the Rayleigh problem** for $f_{\max} = 20, c_{L,f_{\max}} = 0.5, \delta = \lambda/64$, in a wind $W(z) = W_0 \left(2 + \frac{1}{1+\exp{-z/\delta}} \right)$. The constant term in the wind definition, while having no effect on air-relative quantities, illustrates how the trajectory is overall convected downwind if the slow layer has a non-zero velocity.